TECHNICAL ARTICLE

Microstructure Evolution and Recrystallization Mechanisms of High Mg Alloyed Al-Mg Alloy during Friction Stir Welding with Different Cooling Media

Tian Ding, Hongge Yan, Jihua Chen, Weijun Xia, Bin Su, and Huaming Zhu

Heat input in friction stir welding (FSW) plays a vital role in determining the microstructure of the weld joint. Microstructure evolution and recrystallization mechanisms of high Mg alloyed Al-Mg alloy (Al-9.2 Mg-0.8Mn-0.2Zr-0.15Ti) during FSW with natural cooling and water cooling are carefully investigated by SEM, TEM and EBSD. Compared with natural cooling, water cooling can refine grain size and produce the higher fraction of high-angle grain boundaries (HAGBs) and lower texture intensity in the stir zone (SZ) but generate the lower fractions of HAGBs in the thermo-mechanically affected zone (TMAZ) and heat-affected zone (HAZ) and the higher texture density in the HAZ of the weld joint. The dispersed Al_6Mn phases and some broken Al_6(Fe, Mn) particles are existent in the SZ of both FSWed joints, while the β-Al_3Mg_2 phase is dissolved in the SZ due to the frictional heat. Continuous dynamic recrystallization (CDRX) and dynamic recovery (DRV) are the main mechanisms of microstructure evolution in the SZ of both FSWed joints. CDRX occurs in the TMAZ of the joint with natural cooling, while discontinuous dynamic recrystallization (DDRX) occurs in that with water cooling. Static recovery (SRV) and continuous static recrystallization (CSRX) are the main mechanisms of microstructure evolution in the HAZ of the joint with natural cooling, while the microstructure evolution in the HAZ of the joint with water cooling includes SRV and discontinuous static recrystallization mechanism (DSRX).

Keywords	Al-Mg alloy, friction stir welding, microstructure evolution, water cooling

1. Introduction

Al-Mg series aluminum alloys with medium and low Mg contents have broad application prospects in aerospace, automobile, shipbuilding and other fields due to their low density, moderate strength, good ductility, excellent corrosion resistance and so on (Ref 1). The strength is mainly achieved by solid solution strengthening and strain hardening. Thus, the increase in Mg content can improve the strength and thus expand the applications in the engineering field. The welding processes are essential to manufacture various large-size complex parts in the industrial field. Some defects such as Mg element evaporation, porosity, solidification cracking, large welding distortion and segregation are involved in the high Mg alloyed Al-Mg alloy joints prepared by the conventional fusion welding processes and thus result in the lower mechanical properties of the joints (Ref 2). However, FSW, as a green and environmentally friendly solid-state joining technique, has been successfully

used in joining Al-Mg alloys, which can avoid many welding defects caused by the conventional fusion welding processes and thereby improve the mechanical properties of the joints. The microstructure evolution during FSW plays a vital role in determining the mechanical properties of the joint. However, the microstructure evolution of the high Mg alloyed Al-Mg alloys during FSW especially with water cooling have been scarcely reported yet.

Up to now, some studies have been conducted on the microstructure and mechanical properties of the FSWed Al-Mg joints with medium and low Mg contents. For example, Hao et al. (Ref 3) have studied the FSWed Al-5.7 Mg-0.6Mn-0.1Zr-0.3Er (wt.%) alloy joints and have found that the SZ are consisted of fine equiaxed recrystallization grains and low dislocation density in comparison with the cold-rolled base metal (BM). In addition, Chen et al. (Ref 4) have investigated the FSWed 5A06 Al alloy joints and pointed out that in addition to fine equiaxed grains, the round β-Al_3Mg_2 phases and the small plate-shaped Al_6(Fe, Mn) particles are partially dissolved in the SZ. Moreover, water cooling is used to inhibit grain growth during FSW so as to improve the joint strength (Ref 5-8). For example, Wang et al. (Ref 5) have achieved the FSWed 5083-H19 aluminum alloy joints with the similar fatigue strength to the BM and have reported that in-process with water cooling can obtain more ultrafine grains with higher dislocation density in the SZ and the weaker softening effect in the HAZ than natural cooling. Singh et al. (Ref 6) also have studied the cooling environment effect on the microstructure and mechanical properties of the FSWed AA 5052 strain-hardenable aluminum alloy and have found that water cooling brings about the finer grain size in the SZ and the narrower widths of

Tian Ding, Hongge Yan, Jihua Chen, Weijun Xia, and **Bin Su**, School of Materials Science and Engineering, Hunan University, Changsha 410082, People's Republic of China; and **Huaming Zhu**, Trio Metal (GZ) Co., Ltd, Guangzhou, People's Republic of China. Contact e-mails: dingtian@hnu.edu.cn, yanhg68@163.com, and jihuachen@hnu.edu.cn.

the SZ, TMAZ and HAZ. Mehta et al. (Ref 7) have investigated conventional and cooling assisted friction stir welding of AA6061 and AZ31B alloys. The results have pointed out that the tensile strength of the dissimilar joints is enhanced by cooling assisted welding process due to the reduction in the number of intermetallic compounds inside the weld bead. Mofid et al. (Ref 8) have researched that the effect of water cooling during dissimilar friction stir welding of 5083 alloy to AZ31 alloy. They have found that the SZ with water cooling shows a much smoother interface and less intermixing, but water cooling does not improve the hardness of the joint. However, these studies mainly focus on the microstructure evolution in the SZ of the FSWed joint and few studies on the microstructure evolution in the TMAZ and HAZ during FSW of Al-Mg alloy with high Mg content. It is generally recognized that both the TMAZ and HAZ are the dominant tensile fracture locations of the FSWed joints (Ref 3, 9, 10). Therefore, microstructure optimization of the TMAZ and HAZ is of great significance to improve mechanical properties of the FSWed joint.

So far, the microstructure evolutions in the SZ of the FSWed low and medium Mg alloyed Al-Mg alloy joints with different cooling conditions have been investigated, but the microstructure evolutions and the related mechanisms of high Mg alloyed Al-Mg alloys during FSW remain unclear. Especially, there is lack of the systematic study about the effect of water cooling on grain size, the fraction of HAGBs, texture characteristics and precipitation feature of the different welding zones in the FSWed high Mg alloyed Al-Mg alloy joint and the related mechanisms. Whether water cooling brings about the beneficial effect on the FSWed joint of the high Mg alloyed Al-Mg alloy or not is worthy of being further studied. Therefore, the cold-rolled Al-9.2 Mg-0.8Mn-0.2Zr-0.15Ti alloy sheets with the thickness of 2 mm are selected to study and clarify the microstructure evolutions and the related mechanisms in the SZ, TMAZ and HAZ of the joints with different cooling conditions, which will lay the foundations for the achievement of the high-quality FSWed joints.

2. Experimental Details

The cold-rolled Al-9.2 Mg-0.8Mn-0.2Zr-0.15Ti sheet with the thickness of 2 mm was selected for the present study. Before rolling, a homogenization process (400 °C/24 h) was conducted to achieve the homogenous distribution of the micro-alloying elements, especially Mg within the grains. FSW was conducted at the rotation speed w of 1500 rpm and the welding speed v of 75 mm/min. The welding tool was made of H13 tool steel and consists of a shoulder with the diameter of 10 mm and the conical threaded pin with the tip diameter of 3.6 mm, the root diameter of 2.5 mm and the length of 1.8-1.9 mm. The tool was tilted by 2.5° from the normal of the sheet and the tool plunge depth maintains the level of 0.15 mm during welding. The FSWed joints with natural cooling and water cooling were encoded as NC and WC, respectively.

Microstructure of the BM was observed by a LeitzMM-6 optical microscopy (OM). The cross-sectional macrographs of the joints perpendicular to the welding direction were recorded by a Keyence VHX-5000 ultra-depth three-dimensional stere-omicroscope. The specimens for OM observation were ground, polished and then etched by the Keller's reagent (2 mL

HF + 3 ml HCl + 5 ml LNO$_3$ + 190 ml Listilled water) for 60-90 s. The second phase particles in the BM were analyzed by a Tescan Mira4 scanning electron microscope (SEM) equipped with Oxford x-ray energy dispersive spectroscopy (EDS). Electron backscatter diffraction (EBSD) analysis was conducted on a FEI Quanta 2000 SEM at the operating potential of 20 kV. Sub-structures and precipitates of the joint were characterized by a Thermo Scientific, Themis Z transmission electron microscopy (TEM). The samples for EBSD and TEM were prepared by electron-polishing and twin-jet electron-polishing in a mixture of 70% CH$_3$OH + 30% HNO$_3$ at 15 V and − 30 °C, respectively.

3. Results

3.1 Microstructure of BM

The optical images of the BM at different planes are shown in Fig. 1. RD, TD and ND stand for rolling direction, transverse direction, and normal direction, respectively. The cold-rolled sheet exhibits a typical deformed microstructure, with the elongated grains of ∼ 72 μm in length and ∼ 7 μm in thickness. The grains are pancake shaped in the rolling plane (Fig. 1a), in irregular shapes in the transverse cross-sectional plane (Fig. 1b), and strip-like in the longitudinal cross-sectional plane (Fig. 1c).

TEM and SEM images along with EDS mapping of the BM are shown in Fig. 2. As shown in Fig. 2(a), the Al$_6$(Fe, Mn) phase is the main residual second phase, and it cannot be completely dissolved into α-Al during the solution treatment due to its high melting point (higher than 600 °C) [11]. Moreover, some particles rich in Si and Mg are detected and these particles are also difficult to be dissolved into α-Al during the solution treatment, which is shown in Fig. 2(b). These impurity elements such as Fe and Si are induced by the alloy metallurgy process. As shown in Fig. 2(c), the high-density dislocations and some precipitates are observed in the cold-rolled alloy, which indicating that the dislocation strengthening is the most important way of strengthening in the BM.

3.2 Microstructure of the FSWed Joint

3.2.1 Macrographs of the Joints. The sound defect-free FSWed joints of the cold-rolled high Mg alloyed Al-Mg alloy are obtained and their cross-sectional macrographs are shown in Fig. 3. Affected by the shoulder and the pin, the weld zone is generally basin shaped, widening at the top and narrowing at the bottom. Furthermore, the boundary between TMAZ and SZ at the advancing side (AS) is more prominent and sharper than the retreating side (RS), which is attributed to the higher heat input in the AS compared with the RS and the different plastic flow states of the metals on both sides during the FSW process (Ref 4, 12).

Moreover, the widths of SZ, TMAZ and HAZ are different for two kinds of joints. The widths of SZ are approximately 3.2 mm for both joints, but the widths of TMAZ and HAZ are different, which are shown in Fig. 4. In the TMAZ, the peak temperature decreases with the distance from the weld line from ∼ 0.7 to 0.6 T_m. In the HAZ, the peak temperature decreases gradually from ∼ 0.55 T_m to ambient temperature from the TMAZ to the BM (Ref 13). The higher heat input would be generated in the AS during FSW (Ref 4); thus, the
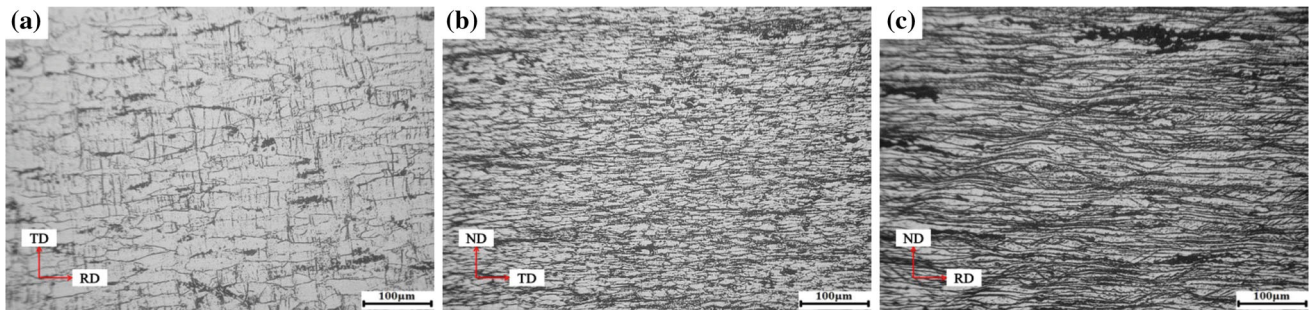
Fig. 1 Optical images of the BM at different planes: (a) the rolling plane, (b) the transverse cross-sectional plane, (c) the longitudinal cross-sectional plane
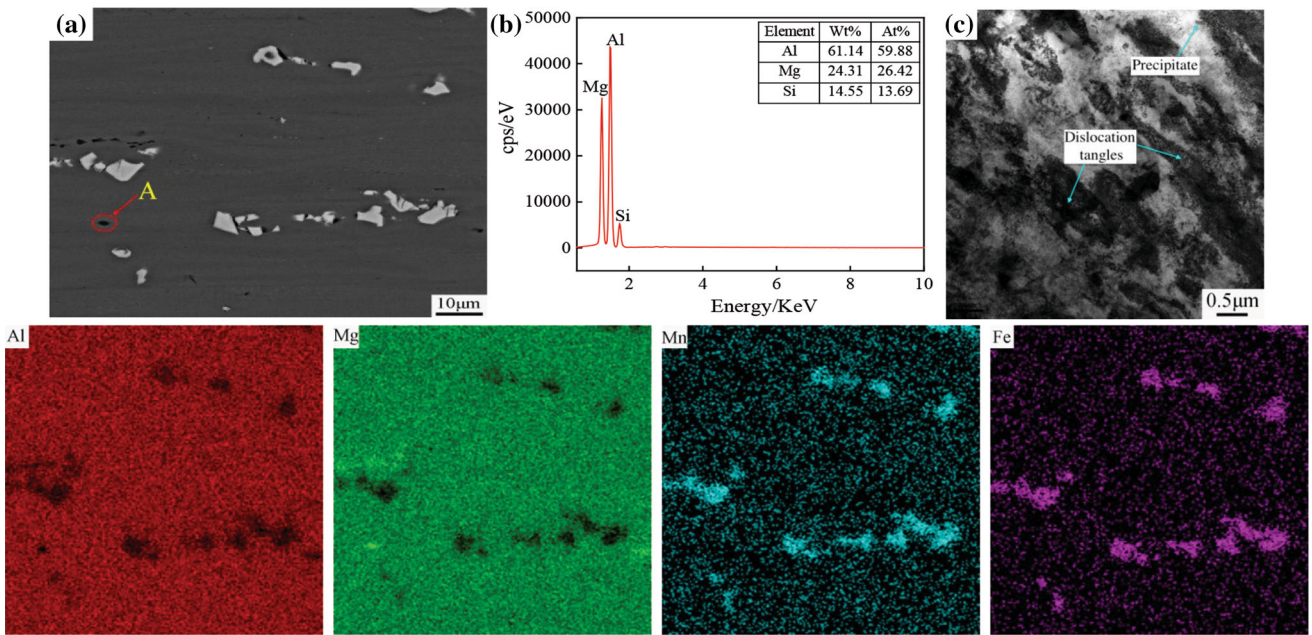

Fig. 2 TEM and SEM images along with EDS mapping of the BM. (a) The residual second phase particles; (b) EDS of particle A; (c) Dislocations and precipitates
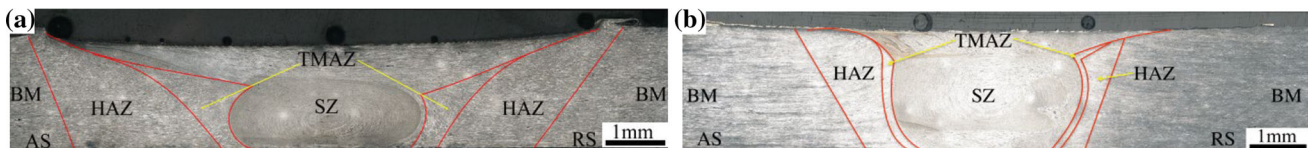

Fig. 3 The cross-sectional macrographs of the FSWed joints: (a) NC; (b) WC

widths of TMAZ and HAZ at the AS are larger than the counterparts of TMAZ and HAZ at the RS. In addition, although the temperature of the TMAZ is higher than that in the HAZ, the strain rate range of the TMAZ is narrow, so the width of the TMAZ is lower than that of the HAZ. Furthermore, water cooling can reduce the peak temperature and thus minimize the softening extent of the joint (Ref 14). Therefore, the widths of HAZ and TMAZ are reduced in comparison with the NC joint.

3.2.2 Microstructure of the SZ. IPF maps, DRX grain sizes and misorientation angle distribution states in the SZ of both joints are shown in Fig. 5. In comparison with BM, grain refinement in the SZ is related to the stirring effect of the stir pin that leads to DRX due to the concurrent effects of frictional heat and plastic deformation, which are shown in Fig. 5(a, d). As seen from Fig. 5(b, e), the average DRX grain sizes in the SZ with natural cooling and water cooling are 3.1 and 1.2 μm, respectively. As seen from Fig. 5(c, f), the fractions of HAGBs (misorientation angle $\geq 15°$) in the SZ with natural cooling and water cooling are 91.2 and 96.2%, respectively.

The DRX grain size in the SZ is mainly related to the two key parameters including strain rate $\dot{\varepsilon}$ (s^{-1}) and peak temperature T (K) during FSW. The lower T and the higher $\dot{\varepsilon}$ result in the finer DRX grains (Ref 15). This effect can be expressed by the Zener-Hollomon parameter Z (s^{-1}).

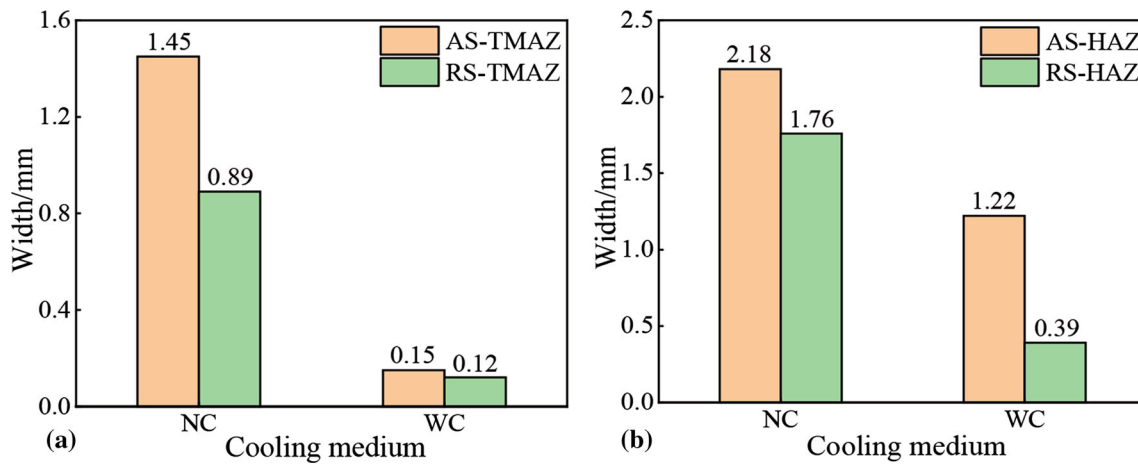$$Z = \dot{\varepsilon} \exp\left(\frac{Q}{RT}\right) \qquad (\text{Eq 1})$$

Fig. 4 The widths of TMAZ (a) and HAZ (b) for both joints
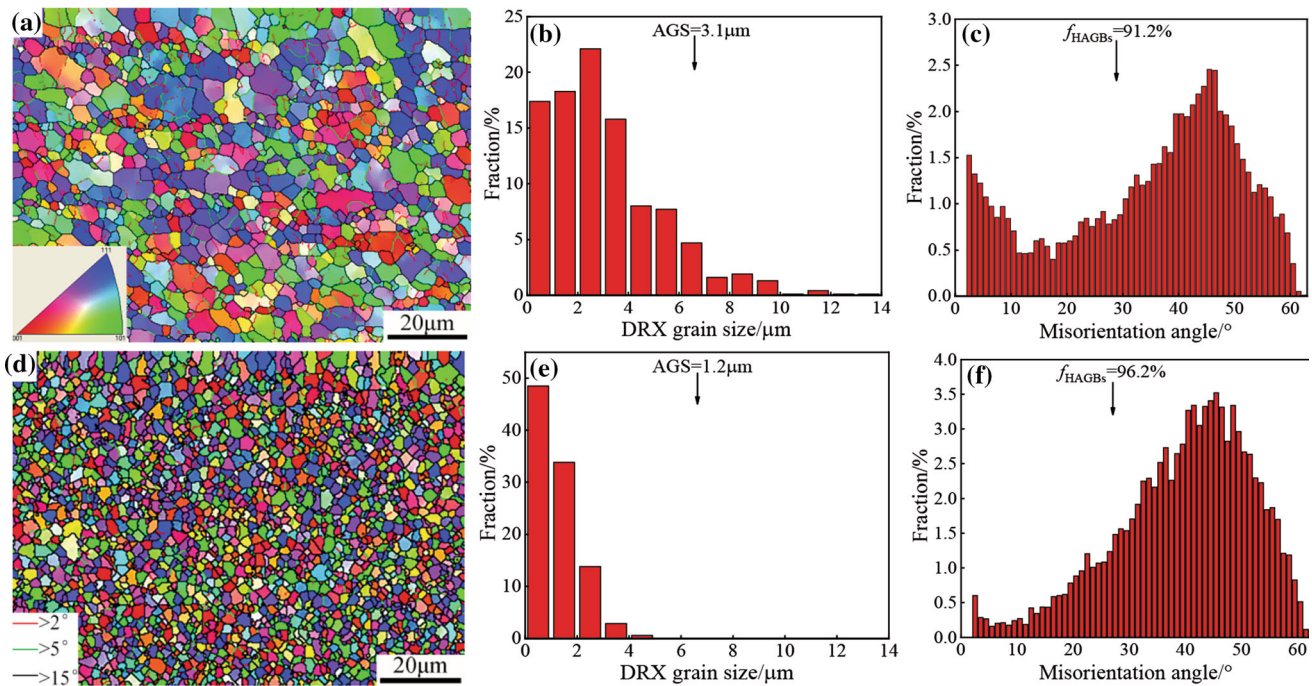

Fig. 5 IPF maps, DRX grain sizes and misorientation angle distributions in the SZ of two joints (AGS is the average DRX grain size): (a), (b), (c) NC; (d), (e), (f) WC

where Q is activation energy (129.66 kJ/mol) and R is gas constant (8.31 J/(mol·K)) (Ref 15). Thus, the higher $\dot{\varepsilon}$ and the lower T represent the higher Z value and the latter means the finer DRX grain size.

The strain rate $\dot{\varepsilon}$ in the SZ can be estimated according to the following equation (Ref 15),

$$\dot{\varepsilon} = k \frac{\pi w r_e}{L_e} \qquad (Eq\ 2)$$

where r_e and L_e are the radius and depth of the DRX region, respectively; w is the rotation speed and k is a constant that depends on the material characteristics and the tool geometry. The r_e and L_e are almost the same under the same rotation speed and welding speed in the present study, and thus the strain rate is basically the same under the same position and rotation speed. Therefore, the change of Z parameter mainly

depends on the temperature (T). As mentioned above, water cooling is associated with the lower peak temperature, resulting in the higher Z value and thereby leads to the finer DRX grain in the SZ.

The fine grains with a high fraction of HAGBs in the SZ are produced by DRX owing to the heat effect and the plastic deformation during FSW. As seen from Fig. 5(c, f), a high fraction of HAGBs are obtained in the SZ of both joints and the joint with water cooling has a higher fraction of HAGBs than that with natural cooling. Moreover, the grain boundary misorientation angles of both joints are in random distribution, indicating that the texture of the SZ is weakened. To further confirm this point, the pole densities in the SZ of both joints are collected. As shown in Fig. 6, the maximum texture densities of the joint with natural cooling and water cooling are 2.46 and 1.53, respectively, indicating that the in-process with water
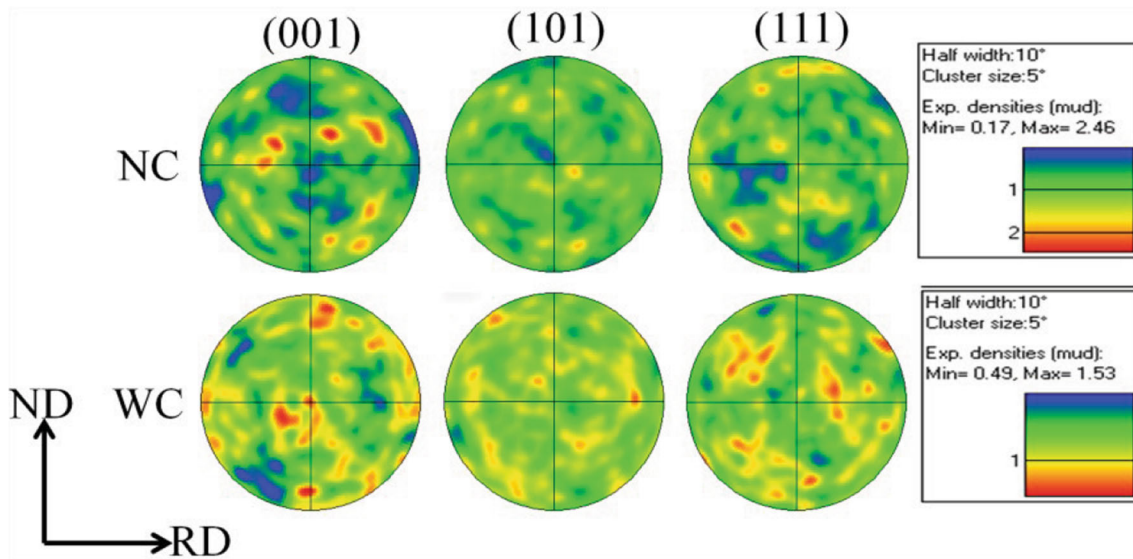
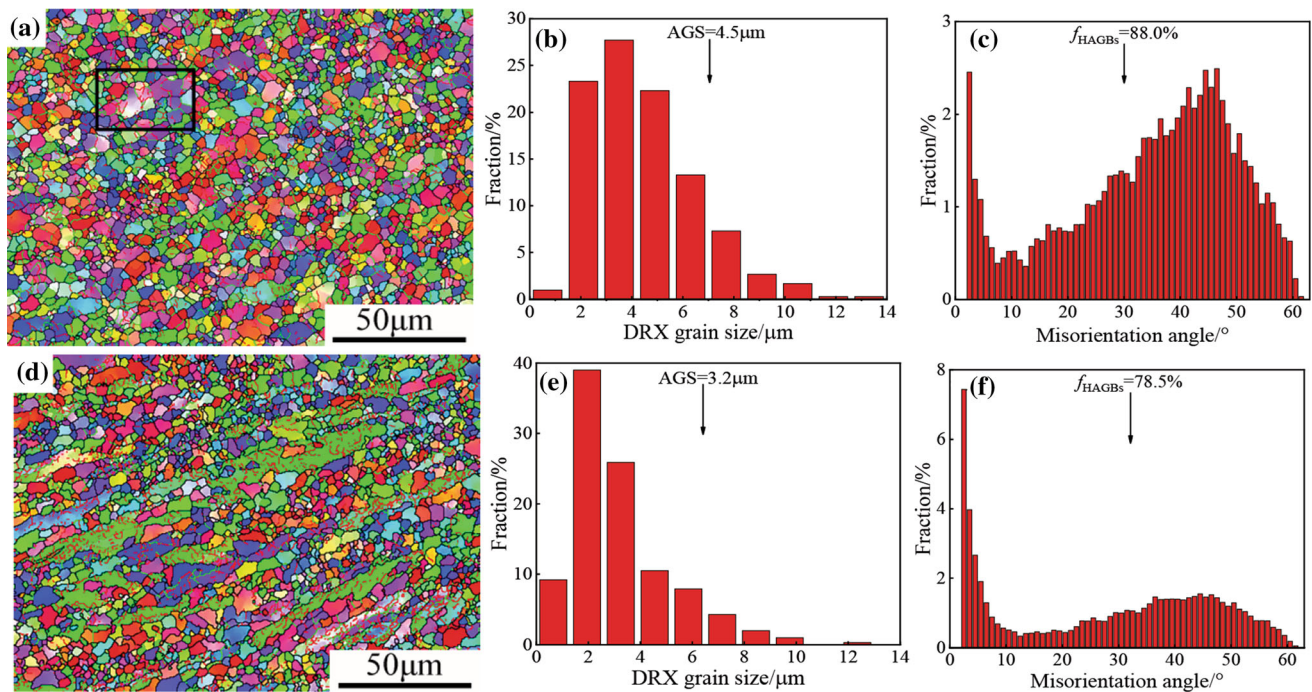**Fig. 6** The pole diagrams in the SZ of both joints

Fig. 7 IPF maps, DRX grain sizes and misorientation angle distribution states of the microstructures in AS-TMAZ for both joints: (a), (b), (c) NC; (d), (e), (f) WC

cooling can refine the DRX grain size and thus weaken the texture in the SZ.

3.2.3 Microstructure of the TMAZ. TMAZ lies between the HAZ and the SZ, which experiences the lower heating temperature and the smaller plastic deformation degree than the SZ. Therefore, it has different microstructure from BM, HAZ and SZ. IPF maps, DRX grain sizes and misorientation angle distribution states of the microstructures in the TMAZ at the AS (AS-TMAZ) and the TMAZ at the RS (RS-TMAZ) for both joints are shown in Fig. 7 and 8, respectively.

As seen from Fig. 7 and 8(a, d), the DRX process is suppressed in the TMAZ during FSW by water cooling. Water

cooling is an effective strategy to reduce the peak temperature and shorten the holding time of the peak temperature (Ref 14). Some un-DRXed regions are existent in the TMAZ. The average DRX grain sizes in the AS-TMAZ with natural cooling and water cooling are 4.5 and 3.2 μm, respectively, while those in the RS-TMAZ with natural cooling and water cooling are 4.3 and 3.0 μm, respectively. Obviously, the average DRX size in the AS-TMAZ is larger than that in the RS-TMAZ of both joints, and in-process with water cooling can refine the DRX grain size in the TMAZ. In addition, the fractions of HAGBs in the AS-TMAZ with natural cooling and water cooling are 88.0 and 78.5%, respectively, while those in the RS-TMAZ are 87.7
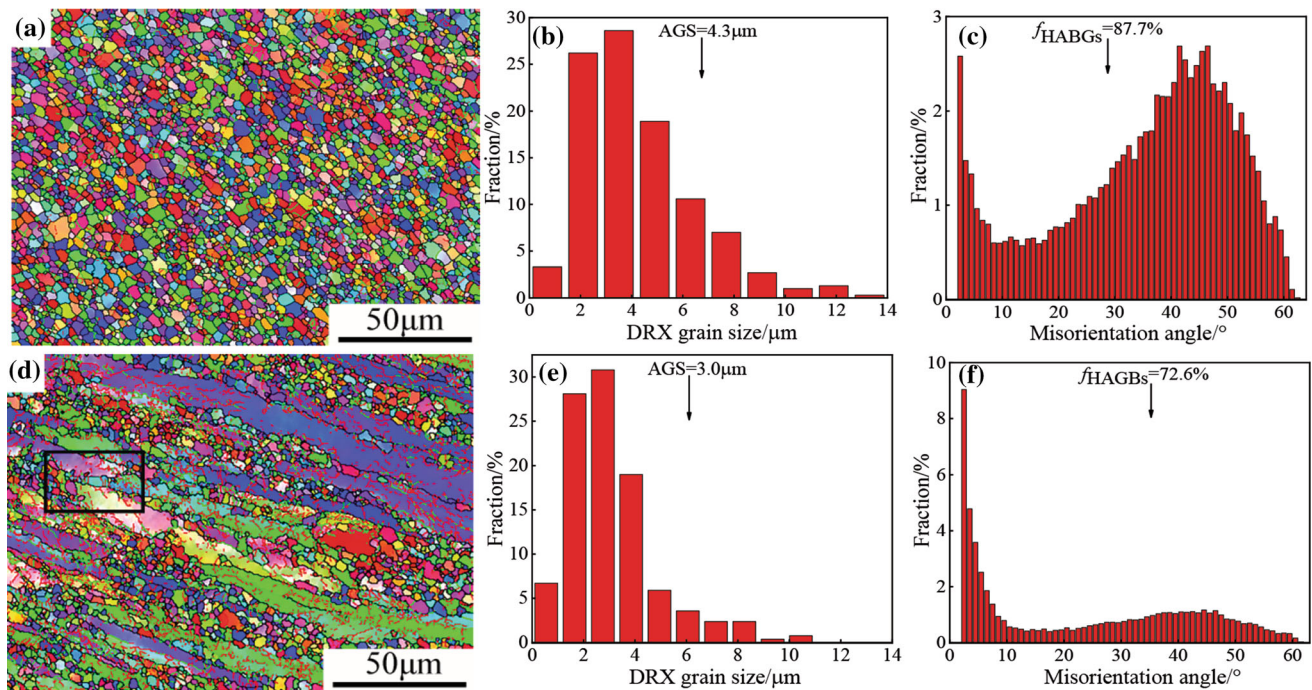
Fig. 8 IPF maps, DRX grain sizes and misorientation angle distribution states of the microstructures in RS-TMAZ for both joints: (a), (b), (c) NC; (d), (e), (f) WC

and 72.6%, respectively. The fraction of HAGBs in the TMAZ with water cooling is lower than that in the TMAZ with natural cooling due to the un-DRXed region involves the higher dislocation density.

3.2.4 Microstructure of the HAZ. The material in the HAZ is subjected to the frictional heat but experiences no plastic deformation. Therefore, the temperature in the HAZ is lower than that in the TMAZ, while the frictional heat still has a significant effect on the microstructure and mechanical properties. The microstructure change in the HAZ includes dissolution and coarsening of precipitates, recovery, recrystallization, and grain growth (Ref 16). IPF maps, DRX grain sizes and misorientation angle distribution states of the microstructures in HAZ for both joints are shown in Fig. 9. As seen from Fig. 9(a, d), the static recrystallization (SRX) occurs in the HAZ due to the frictional heat. As seen from Fig. 9(b, e), the average SRX grain sizes in the HAZ with natural cooling and water cooling are 6.4 and 3.4 μm, respectively. As seen from Fig. 9(c, f), the fractions of the HAGBs in the HAZ with natural cooling and water cooling are 86.4 and 76.4%, respectively.

Since the lower peak temperature and the shorter duration at high temperatures are associated with water cooling, SRX proceeds adequately in the HAZ of the joint with natural cooling, however, the finer SRX grain size and the lower HAGBs are involved in the HAZ of the joint with water cooling. The pole diagrams in the HAZ of both joints are shown in Fig. 10. The maximum texture densities of the joint with natural cooling and water cooling are 2.78 and 4.71, respectively. Generally, the more sufficient of the recrystallization is, the weaker of the texture is. Therefore, the higher texture intensity appears in the HAZ of the joint with water cooling. In addition, compared with the SZ, the maximum texture density in the HAZ increases significantly, especially for the water cooling condition. Water cooling reduces the peak temperature, which leads to the decrease in recrystallization degree in the HAZ and thus increase the texture strength.

4. Discussion

4.1 Evolution of Grain Size and Fraction of HAGBs in the FSWed Joint

Grain sizes and the fraction of HAGBs in the different zones of two FSWed joints are shown in Fig. 11. Different microstructure characteristics are involved due to each region experiences different strain rate and welding thermal cycle (Ref 13). According to Fig. 11(a), the grain size in the WC joint is smaller than that in the NC joint since water cooling can increase cooling rate and reduce the peak temperature. The lower peak temperature can inhibit dynamic recovery and promote dynamic recrystallization nucleation, resulting in the finer dynamic recrystallized grains. In addition, the grain size increases in order of the SZ, AS-TMAZ, RS-TMAZ, HAZ for the NC joint and the WC joint. The DRX grain size in the SZ is smaller than that in the TMAZ. The main reason is owing to the larger strain rate in the SZ, which leads to the higher DRX nucleation rate and thereby obtains a smaller DRX grain size. The DRX grain size in the AS-TMAZ is larger than that in the RS-TMAZ, which is ascribed to the higher input in the AS [4]. The SRX grain size in the HAZ is bigger than the DRX grain size in the SZ and TMAZ since no plastic deformation is involved in HAZ.

As shown in Fig. 11(b), the fraction of HAGBs in the SZ with water cooling is higher than that with natural cooling since water cooling suppresses the dynamic recovery, accelerates the DRX process during FSW, and inhibits the growth of dynamic recrystallized grains. The smaller DRX grain size means the higher fraction of HAGBs. However, the fractions of HAGBs
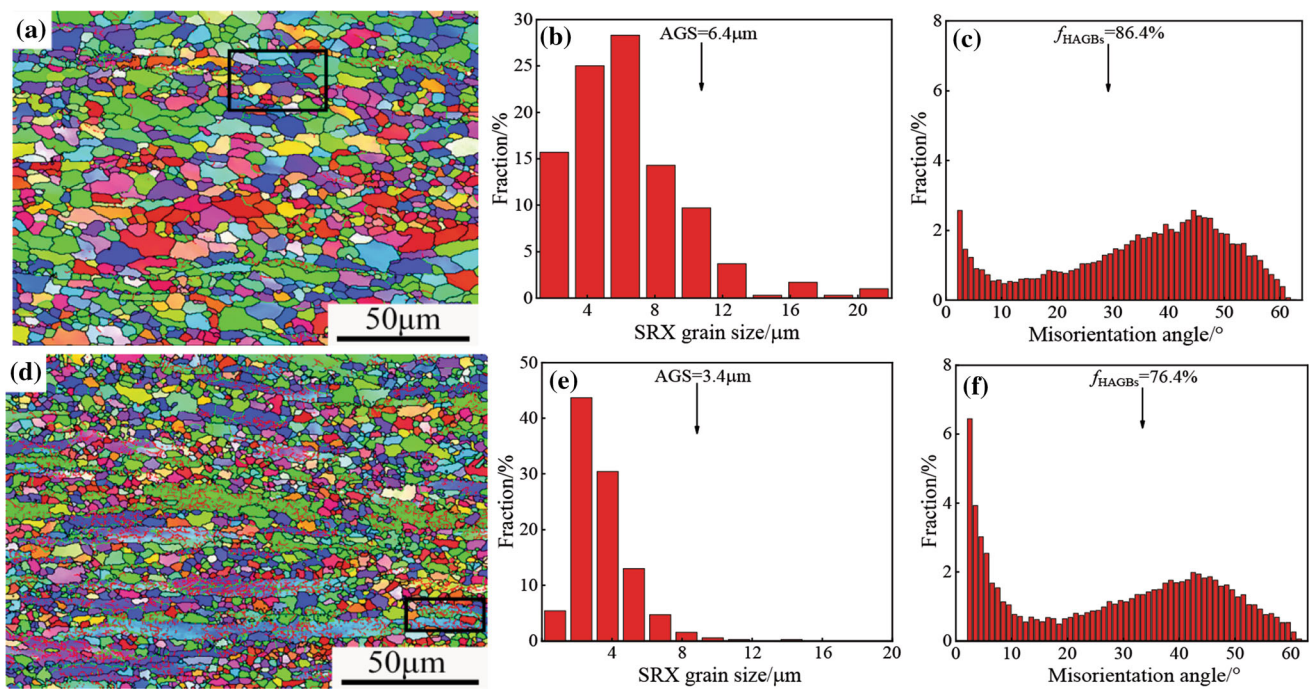
Fig. 9 IPF maps, DRX grain sizes and misorientation angle distribution states of the microstructures in HAZ for both joints: (a), (b), (c) NC; (d), (e), (f) WC
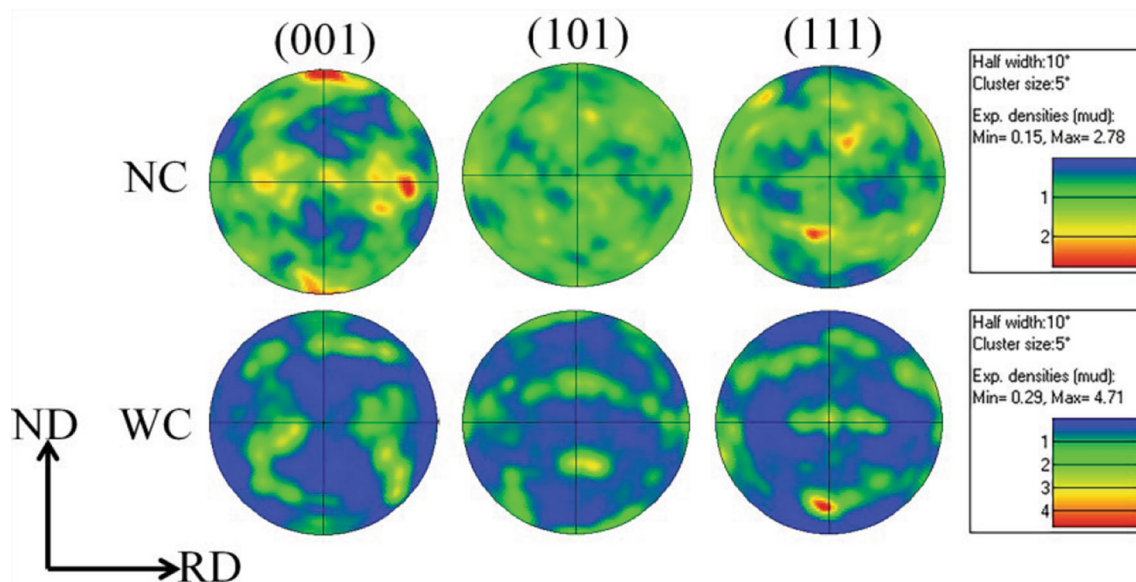

Fig. 10 The pole diagrams in the HAZ of both joints

in both TMAZ and HAZ of the joint with water cooling are lower than the counterparts with natural cooling since water cooling reduces the peak temperature and makes full recrystallization difficult, and thereby some un-recrystallization deformed regions are retained in both TMAZ and HAZ. These un-recrystallization deformed regions contain many low-angle grain boundaries (LAGBs).

4.2 Evolution of Precipitates in the FSWed Joint

Precipitates in the SZ of both joints are shown in Fig. 12. Figure 12(b) is a high magnification image of the red rectangle area in Fig. 12(a). As shown in Fig. 12(a), many precipitates in different shapes are distributed in the SZ of the joint with natural cooling. The precipitates within grains can hinder the dislocations movement, while those at the grain boundaries can inhibit the grain growth.

For clear understanding of the precipitates composition, the elemental mappings are conducted. As shown in Fig. 12(b and c), some fine precipitates contain Mn, while some second phase particles contain Fe. Except for the small residual irregular-shaped Al_6(Fe, Mn) particles, which are broken by the severe shearing force during FSW, some fine rod-shaped Al_6Mn particles are occurred in the SZ of both joints. However, our
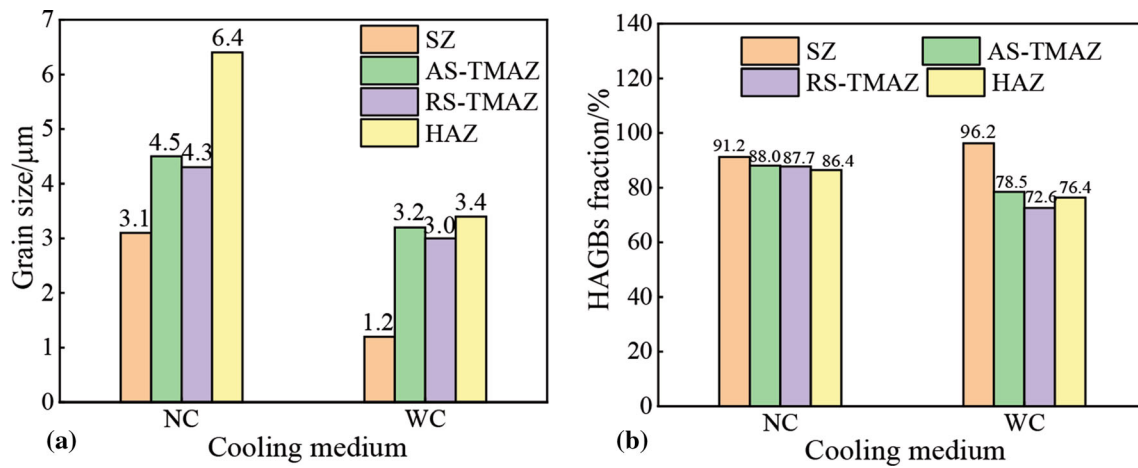
Fig. 11 Grain sizes (a) and the fraction of HAGBs (b) in the different zones of both joints
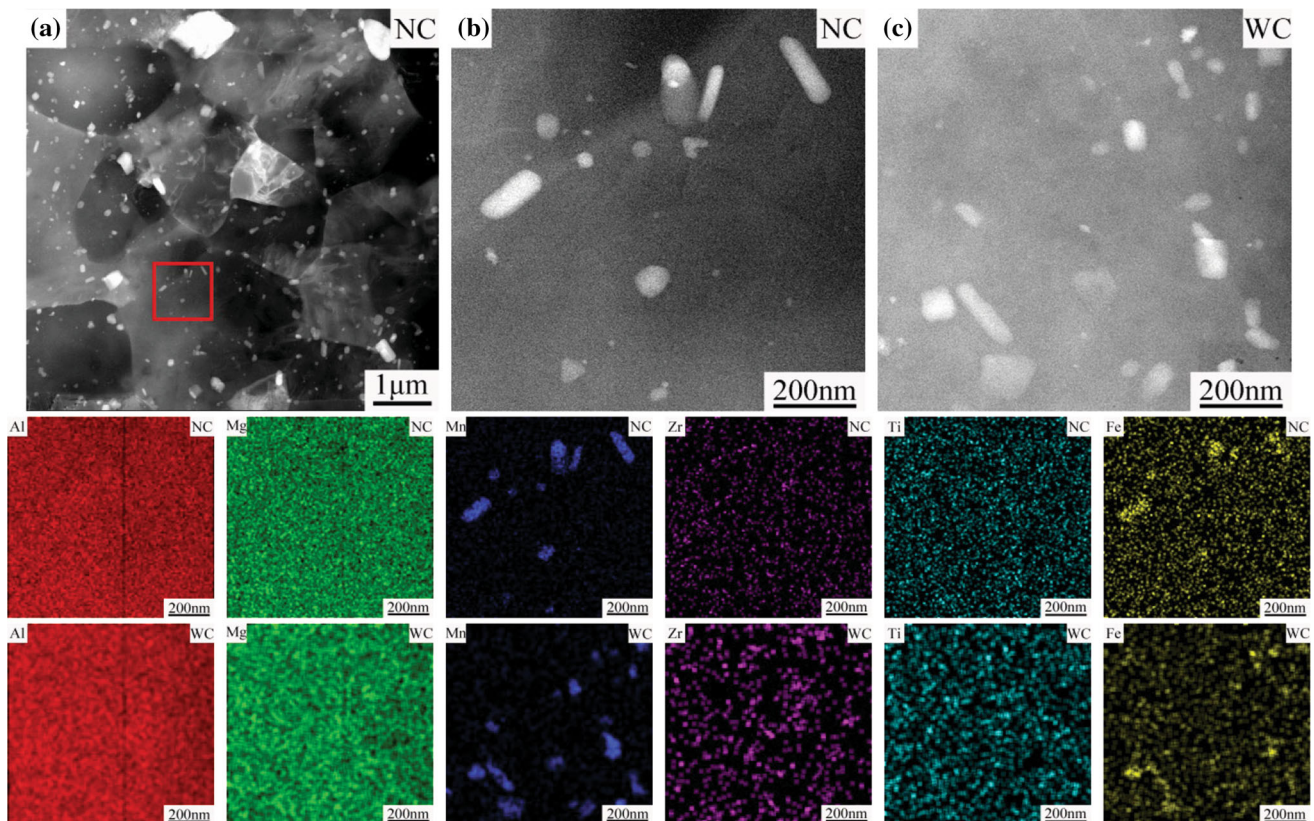

**Fig. 12** Precipitates in the SZ of both joints: (a) and (b) NC; (c) WC

previous study has shown that the β-Al$_3$Mg$_2$ phase occurs in the BM during rolling (Ref 17). Therefore, it can be inferred that the frictional heat during FSW results in the dissolution of β-Al$_3$Mg$_2$ in the SZ. Chen et al. (Ref 4) have reported that the β-Al$_3$Mg$_2$ phase can be dissolved in the SZ of the FSWed 5A06 aluminum alloy joints at the rotation speeds of 700 rpm and 800 rpm. Moreover, Wang et al. (Ref 5) have pointed out that in-process with water cooling can inhibit the precipitation of β-Al$_3$Mg$_2$. According to the above experimental results, both natural cooling and water cooling would result in the dissolution of β-Al$_3$Mg$_2$ in the SZ, which can lead to an increase in the corrosion performance of the FSWed joint.

4.3 Recrystallization Mechanisms

FSW is widely used for the welding of aluminum alloys. The microstructure evolution and the associated mechanism during FSW are of great significance. So far, the studies on the microstructure evolution mechanisms of the FSWed aluminum alloy joints focus on the low Mg alloyed Al-Mg alloys. The related mechanisms are summarized in Table 1. In comparison with BM, the microstructure in the SZ is significantly refined and DRX occurs in the SZ and TMAZ during FSW. The DRX mechanisms mainly include CDRX, DDRX, geometric dynamic recrystallization (GDRX) and particle stimulated nucleation (PSN). Since the high Mg content is associated with the

Table 1 Summary of the microstructure evolution mechanisms of aluminum alloys during FSW

Base metal	Cooling medium	Mechanisms SZ	TMAZ	HAZ	Ref
5083-H112 Al (4.5 wt.% Mg)	Water cooling	CDRX	…	…	18
Al-Li-Cu (0.33 wt.% Mg)	Natural cooling	CDRX	…	…	19
7075-T6 Al (2.5 wt.% Mg)	Natural cooling	DRV + DDRX	…	…	20
5251-H14 Al (2.2 wt.% Mg)	Natural cooling	…	CDRX	SRX	21
5251-O Al (2.2 wt.% Mg)	Natural cooling	…	GDRX	…	21
5086-O Al(4.35 wt.% Mg)	Natural cooling	SIBM + PSN	…	…	22
5083 Al as-cast (4.7 wt.% Mg)	Natural cooling	PSN	…	…	23
2219-T6 Al (non Mg)	Water cooling	DRV + CDRX	…	…	24
Al-9.2 Mg-0.8Mn-0.2Zr-0.15Ti	Natural cooling	DRV + CDRX	CDRX	SRV + CSRX	This work
Cold-rolled (9.2 wt.% Mg)	Water cooling	DRV + CDRX	DDRX	SRV + DSRX	
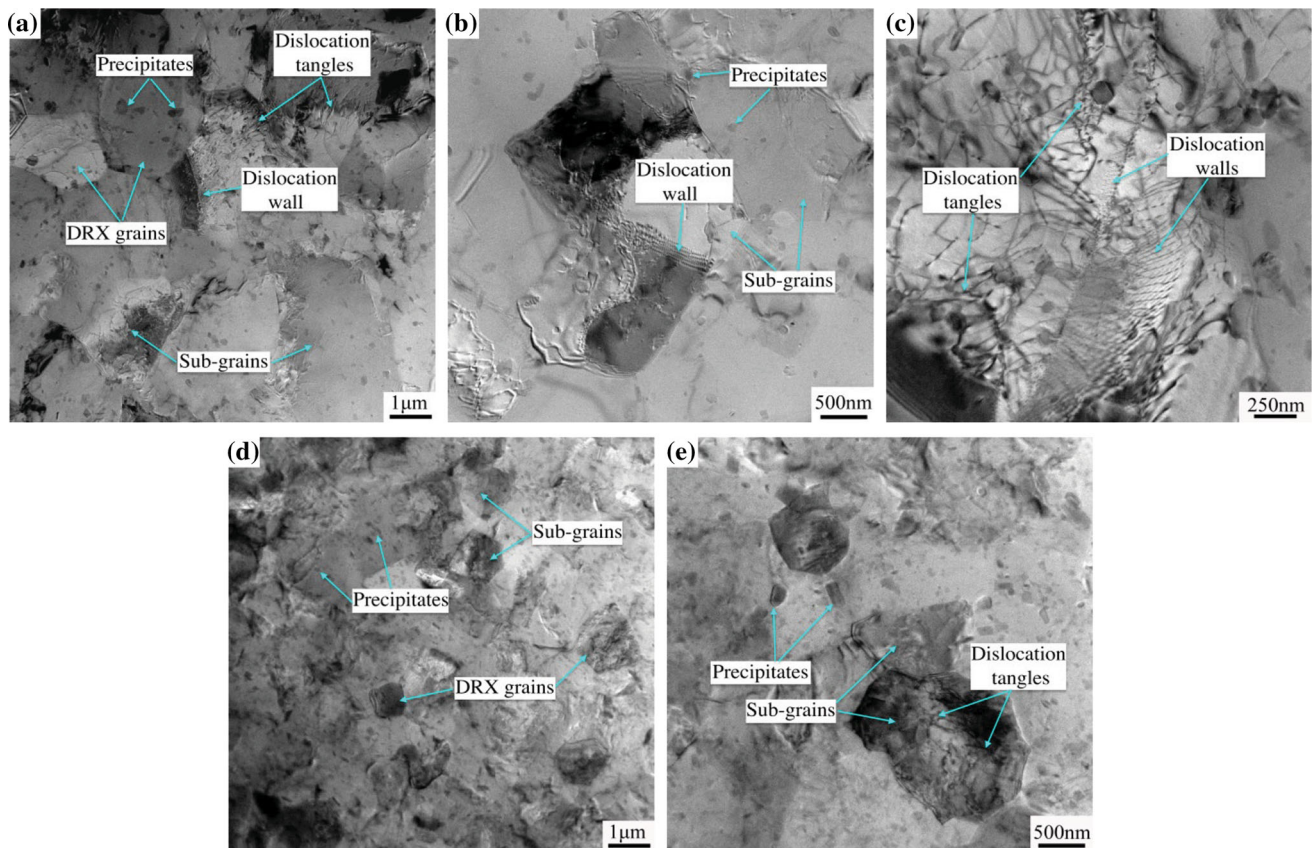
Fig. 13 TEM images of NC (a-c) and WC (d, e) in the SZ

decreased of stacking fault energy (SFE), the DRX behaviors of the FSWed high Mg alloyed Al-Mg alloy joints may be different. To clarify this point, TEM study and EBSD examination are conducted.

During FSW, the original grains are replaced by the fine, equiaxed recrystallized grains in the SZ. TEM images of the SZ for both joints are shown in Fig. 13. Compared with the BM (Fig. 2c), DRX occurs in the SZ of both joints, which is in good consistency with the EBSD results. In-process with water cooling leads to the lower peak temperature and shorten duration at high temperature, thus resulting in the smaller DRX grain size in the SZ (Fig. 13a, d). The SFE of Al-Mg alloy

decreases with the increase in Mg content (Ref 25), and thereby the DDRX mechanism is easy to generate during deformation. Son et al. (Ref 26) have pointed out that the DDRX mechanism is induced in the Al-Mg alloy with the higher Mg content during the hot torsion testing.

However, as shown in Fig. 13, no microstructural evidence shows the formation of the recrystallization nucleation by the grain boundary migration, which are indispensable for the DDRX mechanism. As shown in Fig. 13(b, e), both dislocation tangles and dislocation walls, typical features of CDRX, are detected in the sub-grains. As shown in Fig. 13(b), an ordered dislocation wall alignment occurs within grains to form new

boundaries at the early stage of the sub-grain formation. Dislocations are generated during FSW and gradually absorbed into the sub-grain boundaries. These sub-grains eventually experience rotation and growth to obtain HAGBs. Meanwhile, the sub-grain boundaries are randomly distributed within the grains, which eventually lead to the random distribution of DRX nucleation. It has been reported that strain-induced boundary migration (SIBM) and PSN are the main mechanisms of microstructure evolution in the SZ of Al-Mg alloys with low and medium Mg contents during FSW (Ref 22, 23). However, no relevant mechanisms are found in the present study.

DRV occurs readily during hot working of metals with high SFE such as aluminum, which is owing to the easy initiation of dislocation climb and cross slip (Ref 23). Due to the plastic deformation and the welding thermal cycle, dislocation movement leads to the formation of dislocation tangles and dislocation walls in the original grains, which is indicated by Fig. 13(c). At a certain strain level, dislocation tangles and dislocation walls are transformed into sub-grain boundaries to reduce the total energy of the system, which are indicated by Fig. 13(b, e). This phenomenon is the typical characteristics of DRV. Therefore, CDRX and DRV are the main mechanisms of microstructure evolution in the SZ of both joints.

Though the microstructure evolution mechanisms in the SZ of Al-Mg alloys with low and medium Mg contents have been widely investigated, almost no attention has been paid to the microstructure evolution mechanisms in the TMAZ and HAZ, especially for water cooling. Since only very limited area can be observed by TEM, EBSD study is conducted on TMAZ and HAZ of both FSWed joints. The microstructure evolution mechanisms in the TMAZ of Al-Mg alloys vary with the Mg content and the alloy state. Etter et al. (Ref 21) have reported that CDRX and GDRX occur in the TMAZ of the as-cold rolled and the as-annealed of 5254 aluminum alloy sheets, respectively. However, the microstructure evolution mechanisms in the TMAZ of the FSWed high Mg alloyed Al-Mg alloy joints under both natural cooling and water cooling remain unclear. IPF and KAM distribution maps in the TMAZ of both FSWed joints are shown in Fig. 14. Figure 14(a and b) shows the high magnification images of the rectangle areas in Fig. 7(a) and 8(d), respectively.

According to Fig. 5(d), different misorientation angle distribution of high-angle grain boundaries (HAGBs) ($\theta \geq 15°$) and low-angle grain boundaries (LAGBs) ($\theta < 15°$) are shown with different colors. HAGBs are represented as black line. LAGBs further divided into two categories, one from 2 to 5° represented as red line and the other from 5 to 15° represented as green line. Generally, LAGBs range from 2 to 5° is known as sub-grain boundaries. As seen from Fig. 14(a), the grain

boundaries of the multiple colors indicate that the sub-grain boundaries gradually form into the LAGBs, which are marked by black arrows, and then transform to the HAGBs, indicating that CDRX is the microstructure evolution mechanism in the TMAZ of the joint with natural cooling. As seen from Fig. 14(b), some other interesting microstructure evolution information are revealed in the TMAZ of the joint with water cooling via EBSD analysis. The KAM distribution can reflect the residual dislocation density distribution in the grains. The transition from blue to red in Fig. 14(c) indicates that the KAM increases gradually, which means the higher dislocation density. As seen from Fig. 14(b), the local grain boundary bulging and the growth of the DRX nucleus are observed, which implies that DDRX plays a role in the microstructure evolution during the FSW process with water cooling. Some grains are nucleated by DDRX through the bulging of HAGBs and the migration of boundaries form the bulges, which are surrounded by the LAGBs and are eventually transformed into fine grains. The DDRX nucleus is partially bounded by the bulged portion of the initial HAGB. In-process with water cooling inhibits the recovery process and retains higher density of dislocations in the parent grains, which is shown in the green area in Fig. 14(c). The blue area in Fig. 14(c) indicates that this region has very low density of dislocations. The difference in local dislocation density on both sides of the parent grains is the driving force for the grain boundary migration toward high dislocation density and the corresponding growth of DRX nuclei (Ref 13). Therefore, the bulged grain boundaries can migrate toward the side of parent grains with high dislocation density to obtain the sufficient driving force to grow up. This mechanism is firstly observed in the TMAZ of the FSWed Al-Mg alloy joint with water cooling, which can intensify the knowledge of the microstructure evolution in the TMAZ of the FSWed Al-Mg alloy joint.

Static recrystallization (SRX) is detected in the HAZ of the FSWed Al-Mg alloy joints (Ref 4, 21, 27). However, the related mechanism is not clarified. IPF and KAM distribution maps in the HAZ of both FSWed joints are shown in Fig. 15. Figure 15(a and b) shows the high magnification images of the rectangle areas in Fig. 9(a and d), respectively. Figure 15(c) is the KAM distribution map of Fig. 15(b). As we know, the material is subjected to the frictional heat but no plastic deformation in the HAZ and the peak temperature decreases gradually from ~ 0.55 T_m to room temperature from the TMAZ to BM. Generally, SRV occurs at the temperature higher than $0.3T_m$, while SRX takes actions at the temperature higher $0.4T_m$ (Ref 13). Thus, SRV and SRX are the main microstructure evolution mechanisms in the HAZ. As seen from Fig. 15(a), sub-grain boundaries continuously absorb disloca-
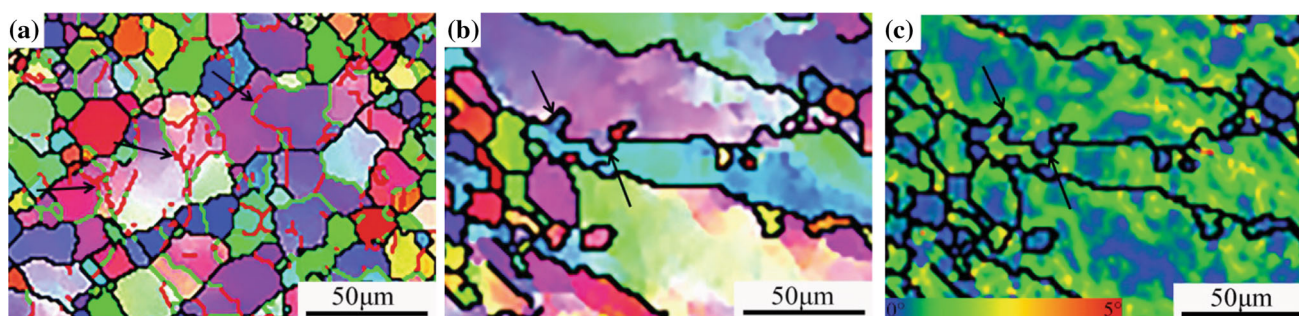

Fig. 14 IPF and KAM distribution maps in the TMAZ of both FSWed joints: (a) NC; (b) and (c) WC
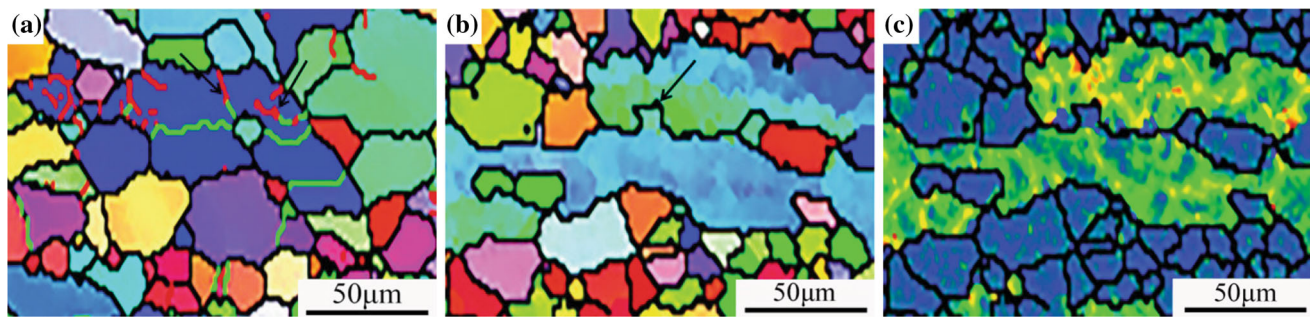
Fig. 15 IPF and KAM distribution maps in the HAZ of both FSWed joints: (a) NC; (b and c) WC

tions to form LAGBs and the complete SRX grains eventually appear under the frictional heat, indicating that continuous static recrystallization (CSRX) is dominant mechanism in the HAZ of the joint with natural cooling. However, discontinuous static recrystallization (DSRX) occurs in the HAZ of the joint with water cooling, which is indicated by Fig. 15(b). DSRX has the similar nucleation mechanism as DDRX. Nucleation proceeds by the migration of the pre-existing HAGBs into the deformed microstructure. The driving force for nucleation is the decrease in energy arising from the dislocations consumed by the migration portion of the HAGBs (Ref 13). Subsequently, the growing grains consume the deformed or recovered microstructure until the material is fully recrystallized.

5. Conclusions

In this paper, the sound FSWed high Mg alloyed Al-Mg alloy joints are obtained by in-processes with natural cooling and water cooling. Microstructure evolutions and related mechanisms of both joints are carefully investigated. The main conclusions are summarized as follows.

(1) Water cooling can significantly reduce the softening effect and refine the grain size of the FSWed joint in comparison with natural cooling. The average grain size in the SZ of the joint with water cooling is 1.2 μm, and the average grain size increases gradually from the SZ to HAZ. In-process with water cooling can produce the higher fraction of HAGBs with 96.2% in the SZ, but the lower fractions of HAGBs in the TMAZ and HAZ compared with natural cooling.

(2) The more randomly distributed weaken texture in the SZ of the joint with water cooling due to finer DRX grain sizes. However, the stronger texture appears in the HAZ of the joint with water cooling, attributable to the insufficient SRX. Meanwhile, the maximum texture density in the HAZ is larger than that in the SZ.

(3) The Al_6Mn phases and some broken $Al_6(Fe, Mn)$ particles are dispersed in the SZ of both joints, while the β-Al_3Mg_2 phases are dissolved in the SZ under the frictional heating.

(4) CDRX and DRV are the main microstructure evolution mechanisms in the SZ of both joints. CDRX occurs in the TMAZ of the joint with natural cooling, while DDRX appears in the TMAZ of the joint with water cooling. SRV and CSRX are the main mechanisms in

the HAZ of the joint with natural cooling, while SRV and DSRX occur in the joint with water cooling.

References

1. T. Hirata, T. Oguri, H. Hagino, T. Tanaka, S.W. Chung, Y. Takigawa, and K. Higashi, Influence of Friction Stir Welding Parameters on Grain Size and Formability in 5083 Aluminum Alloy, *Mater. Sci. Eng. A*, 2007, **456**, p 344–349.

2. Z.B. He, Y.Y. Peng, Z.M. Yin, and X.F. Lei, Comparison of FSW and TIG Welded Joints in Al-Mg-Mn-Sc-Zr Alloy Plates, *Trans. Nonferr. Metal. Soc. China*, 2011, **21**, p 1685–1691.

3. H.L. Hao, D.R. Ni, Z. Zhang, D. Wang, B.L. Xiao, and Z.Y. Ma, Microstructure and Mechanical Properties of Al-Mg-Er Sheets Jointed by Friction Stir Welding, *Mater. Des.*, 2013, **52**, p 706–712.

4. S.J. Chen, X.X. Li, X.Q. Jiang, T. Yuan, and Y.Z. Hu, The Effect of Microstructure on the Mechanical Properties of Friction Stir Welded 5A06 Al Alloy, *Mater. Sci. Eng. A*, 2018, **735**, p 382–393.

5. B.B. Wang, P. Xue, B.L. Xiao, W.G. Wang, Y.D. Liu, and Z.Y. Ma, Achieving Equal Fatigue Strength to Base Material in a Friction Stir Welded 5083-H19 Aluminum Alloy Joint, *Sci. Technol. Weld. Join.*, 2020, **25**(1), p 81–88.

6. R.K.R. Singh, D.W. Rathod, R. Prasad, and S. Pandey, Cooling Environment Effect on the Microstructure and Mechanical Properties of Friction Stir-Welded Joints, *J. Mater. Eng. Perform.*, 2019, **28**, p 3737–3747.

7. K.P. Mehta, P. Carlone, A. Astarita, F. Scherillo, F. Rubino, and P. Vora, Conventional and Cooling Assisted Friction Stir Welding of AA6061 and AZ31B Alloys, *Mater. Sci. Eng. A*, 2019, **759**, p 252–261.

8. M.A. Mofid, A. Abdollah-zadeh, and F. Malek Ghaini, The Effect of Water Cooling During Dissimilar Friction Welding of Al Alloy to Mg Alloy, *Mater. Des.*, 2012, **36**, p 161–167.

9. H.J. Zhang and H.J. Liu, Mathematical Model and Optimization for Underwater Friction Welding of a Heat-Treatable Aluminum Alloy, *Mater. Des.*, 2013, **45**, p 206–211.

10. P. Chen, J. Chen, S.Y. Qin, S.Q. Zou, S.B. Song, T. Jiang, Z.Q. Zhang, Z.H. Jia, and Q. Liu, Friction Stir Welding Joints of 2195-T8 Al-Li Alloys: Correlation of Temperature Evolution, Microstructure and Mechanical Properties, *Mater. Sci. Eng. A*, 2021, **823**, p 141501.

11. X.X. Li, W.J. Xia, H.G. Yan, J.H. Chen, B. Su, M. Song, Z.Z. Li, and Y.L. Li, Dynamic Recrystallization Behaviors of High Mg Alloyed Al-Mg Alloys During High Strain Rate Rolling Deformation, *Mater. Sci. Eng. A*, 2019, **753**, p 59–69.

12. N.T. Kunbhar, S.K. Sahoo, I. Samajdar, G.K. Dey, and K. Bhanumurthy, Microstructure and Microtextural Studies of Friction Stir Welded Aluminium Alloy 5052, *Mater. Des.*, 2011, **32**, p 1657–1666.

13. A. Heidarzadeh, S. Mironov, R. Kaibyshev, G. Çam, A. Simar, A. Gerlich, F. Khodabakhshi, A. Mostafaei, D.P. Field, J.D. Robson, A. Deschamps, and P.J. Withers, Friction Stir Welding/Processing of Metals and Alloys: A Comprehensive Review on Microstructural Evolution, *Prog. Mater. Sci.*, 2021, **117**, p 100752.

14. X.H. Zeng, P. Xue, L.H. Wu, D.R. Ni, B.L. Xiao, K.S. Wang, and Z.Y. Ma, Microstructural Evolution of Aluminum Alloy During Friction Stir

Welding Under Different Tool Rotation Rates and Cooling Conditions, *J. Mater. Sci. Technol.*, 2019, **35**, p 972–981.

15. W.F. Xu, J.H. Liu, D.L. Chen, G.H. Luan, and J.S. Yao, Improvements of Strength and Ductility in Aluminum Alloy Joints Via Rapid Cooling During Friction Stir Welding, *Mater. Sci. Eng. A*, 2012, **548**, p 89–98.

16. A.P. Reynolds, W.D. Lockwood, and T.U. Seidel, Processing-Property Correlation in Friction Stir Welds, *Mater. Sci. Forum*, 2000, **331–337**, p 1719–1724.

17. T. Ding, H.G. Yan, J.H. Chen, W.J. Xia, B. Su, and H.M. Zhu, Effects of Rolling Deformation on Microstructure, Tensile Properties and Corrosion Behaviors of High Mg Alloyed of Al-Mg Alloy, *J. Mater. Eng. Perform*, 2022, **31**, p 2168–2181.

18. G.Q. Huang, J. Wu, and Y.F. Shen, A Strategy for Improving the Mechanical Properties of FSWed Joints of Non-Heat-Treatable Al Alloys Through a Combination of Water Cooling and Particle Addition, *J. Manuf. Process.*, 2018, **34**, p 667–677.

19. K.V. Jata, and S.L. Semiatin, Continuous Dynamic Recrystallization During Friction Stir Welding of High Strength Aluminum Alloys, *Scr. Mater.*, 2000, **43**, p 743–749.

20. J.Q. Su, T.W. Nelson, and C.J. Sterling, Grain Refinement of Aluminum Alloys by Friction Stir Processing, *Philos. Mag.*, 2006, **86**(1), p 1–24.

21. A.L. Etter, T. Baudin, N. Fredj, and P. Penelle, Recrystallization Mechanisms in 5251-H14 and 5251-O Aluminum Friction Stir Welds, *Mater. Sci. Eng. A*, 2007, **445–446**, p 94–99.

22. N. Nadammal, S.V. Kailas, J. Szpunar, and S. Suwas, Restoration Mechanisms During the Friction Stir Processing of Aluminum Alloy, *Metall. Mater. Trans. A*, 2015, **46A**, p 2823–2828.

23. T.R. McNelley, S. Swaminathan, and J.Q. Su, Recrystallization Mechanisms During Friction Stir Welding/Processing of Aluminum Alloys, *Scr. Mater.*, 2008, **58**, p 349–354.

24. H.J. Zhang, H.J. Liu, and L. Yu, Microstructural Evolution and its Effect on Mechanical Performance of Joint in Underwater Friction Stir Welded 2219-T6 Aluminum Alloy, *Sci. Technol. Weld. Join.*, 2011, **5**(16), p 459–464.

25. M. Ueki, S. Horie, and T. Nakamura, Factors Affecting Dynamic Recrystallization of Metals and Alloys, *Mater. Sci. Technol.*, 1987, **3**, p 329–337.

26. H.W. Son, J.C. Lee, C.H. Cho, and S.K. Hyun, Effect of Mg Content on the Dislocation Characteristics and Discontinuous Dynamic Recrystallization During the Hot Deformation of Al-Mg Alloy, *J. Alloy. Compd.*, 2021, **887**, p 161397.

27. Y.L. Li, H.G. Yan, J.H. Chen, W.J. Xia, B. Su, T. Ding, and X.X. Li, Influences of Welding Speed on Microstructure and Mechanical Properties of Friction Stir Welded Al-Mg Alloy with High Mg Content, *Mater. Res. Express*, 2020, **7**, p 076506.